20

Brownian Oscillator Analysis of Molecular Motions in Biomolecules

W. Doster

20.1 Introduction

Dynamic analysis of biomolecules often works by the principle of difference spectroscopy: What is the qualitative difference in structural flexibility of a protein with and without ligand? This method, illustrated elsewhere in this book, is quite useful considering the complexity of biomolecules. Sometimes, however, differences between different samples are easier to obtain than reproducable identical results. This chapter is addressed to students of biophysics, who would like to proceed further. We present a modern statistical analysis of neutron scattering data applied to biomolecules. We start from the simple model of the harmonic oscillator, introduce the visco-elastic oscillator and conclude with a model-independent moment expansion of the density correlation function. To illustrate the method, a number of recent results on protein dynamics are presented. The power of neutron scattering is that it provides, both spectral and spatial, information from which one can reconstruct in principle the microscopic trajectory of labeled particles on a picosecond time scale. Such results can be used to test molecular dynamic simulations of biomolecules, and simulations can be used to interpret the neutron scattering spectra. Since protein–water interactions belong to the most interesting questions that can be approached with neutron scattering, we start with a brief outline on this topic.

20.2 Dynamics of Protein–Solvent Interactions

The nature of protein–solvent interactions is central to most basic questions in molecular biophysics ranging from protein folding, protein–ligand association to desease-related formation of protein aggregates. Biological structures owe their existence to a delicate balance of weak hydrophilic and hydrophobic forces, which are mediated by the solvent [1]. Moreover, proteins are dynamical structures, which undergo continuous thermal motion induced by the

solvent. Dynamic neutron scattering experiments allow probing the protein–water fluctuations on the relevant time scales. In the absence of solvent or in a rigid environment functionally relevant motions are arrested. Water thus acts as a lubricant to protein dynamics. Figure 20.1 shows a neutron scattering spectrum of myoglobin, exposed to three types of environment: vacuum (dehydrated), fully hydrated with D_2O ($0.4\,g\,g^{-1}$) and vitrified in a perdeuterated glucose glass [2].

The wings of the protein spectra appear to be broadened with respect to the resolution function, which is the signature of structural fluctuations on a picosecond time scale. It is obvious that the spectral broadening is more pronounced with the hydrated sample. The excess broadening derives from water-plasticized translational motions of side chains. That the spectra of the dehydrated and the glucose-vitrified protein display a finite and similar width, indicates rotational transitions of side chains, which persist irrespective of the protein environment. From a dynamical point of view, liquids and proteins are radically different, liquids exhibit short-range order and long-range translational diffusion. Molecular displacements in liquids are continuous and isotropic. Proteins in contrast are long-range ordered, but molecular diffusion is short-ranged. Internal displacements are discontinuous, rotational, and anisotropic. The protein–water interaction introduces liquid aspects to otherwise solid-like molecules. Molecular displacements in dense liquids are dominated by short-range repulsive interactions. For a molecule to move also requires that the nearest neighbors have to move. This is a collective phenomenon resembling more a continuous search for escape out of a cage rather than a discontinuous jump across an energetic barrier. By-passing the barrier by collecting sufficient free volume instead of barrier crossing appears to be the dominant diffusion mechanism in the liquid state [3]. The protein–water

AQ: Please check the change of unit for variable "Q" in fig. 20.1 from A to $Å^{-1}$

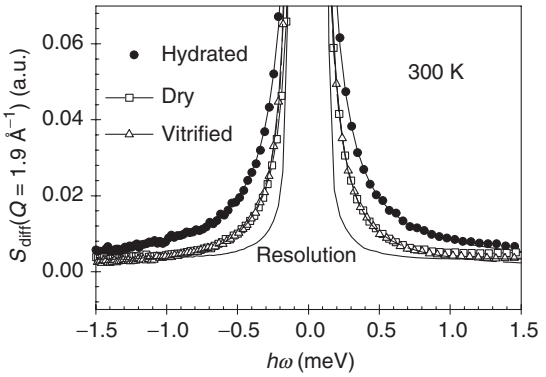

Fig. 20.1. Neutron scattering spectra of diffusive motions at $Q = 1.9\,Å^{-1}$ of myoglobin embedded in three environments as indicated ($1\,meV = 8\,cm^{-1}$). *Full line*: instrumental resolution function (IN6, ILL). A vibrational background was subtracted

interaction causes the protein torsional barriers to fluctuate. The analysis of these motions by dynamic neutron scattering is a classical topic, which has been discussed by many authors, just to cite a small sample [4–6]. The relation between liquids and proteins was discussed in [7–11]. A recent review was published in [12]. The neutron scattering method has the particular advantage to probe the very low frequency range of a few terahertz, where vibrational and relaxational motions overlap. The corresponding spectral features cannot be assigned to vibrations of a particular group. Instead it is dominated by collective motions of many particles. To illustrate the application of neutron scattering to protein–water dynamics we follow a simple physical concept: Protein structural fluctuations are spatially constrained by covalent and van der Waals forces. As a general dynamic model of protein variables. we consider a set of harmonic oscillators which are driven by the random forces of a heat bath, which is essentially the solvent. The generalized protein coordinates X_α then obey a Langevin equation driven by the random forces R_α

$$M_\alpha \ddot{X}_\alpha + f_\alpha \dot{X}_\alpha + \omega_\alpha^2 X_\alpha = R_\alpha(t). \tag{20.1}$$

We thus pick up the basic idea of a normal mode analysis of proteins, complemented by an appropriate frictional force [13,14]. Neutron scattering provides the tools to study the frictional force. In a dynamic neutron scattering experiment, the protein–water hydrogen atoms serve as a monitor to record the trajectory of the X_α in space and time. The theoretical aspects of the application of the Brownian oscillator model to neutron scattering has been discussed by Kneller [15].

20.3 Properties of the Intermediate Scattering Function

An insightful article on the neutron scattering process was written by Mezei [16]. Neutrons are scattered by the nuclei of the atoms, which are point-like entities. The scattered beam pattern is thus determined by the superposition (interference) of spherical waves emitted by the individual atoms. The respective scattering amplitudes depend on the individual nuclear cross-sections, which for C, N, O, H amount to $\sigma_\mathrm{c} = 5.5$, 11.5, 4.2, and 1.76 b ($1\,\mathrm{b} = 10^{-24}\,\mathrm{cm}^2$), respectively [17]. The coherent cross-sections, which specify phase-preserving processes, contribute generally less than 10% to the total scattering intensity with protein samples. Three types of disorder generate an incoherent background (a) chemical disorder, neutron waves scattered by different types of atoms (N, C, H) or isotopes do not interfere; (b) positional disorder, protein powder samples or protein solutions are rotationally disordered, thus waves scattered by identical atoms in different proteins exhibit a random phase relationship; and (c) spin disorder, the neutron cross-section of hydrogen fluctuates depending on whether the respective neutron–proton spins are parallel or antiparallel. The spin-disorder in combination with the

negative scattering length of the proton, lead to a large incoherent cross-section, $\sigma_{\mathrm{inc}} = 80.2\,\mathrm{b}$ [17]. Therefore, roughly 90% of the combined scattering cross-section of D_2O-hydrated protein samples is incoherent. The scattering function $S_{\mathrm{inc}}(Q,\omega)$ thus should be interpreted as the sum of intensities and not as a square of the sum of amplitudes. Finally only those waves can interfere, which originate from one and the same hydrogen atom. This is called "self-interference" and refers to the average behavior of single particles: The motion of the hydrogen atom modulates the phase of the scattered wave (Doppler shift). The self- scattering trace in time thus reflects the trajectory of individual particles. The coherent fraction corresponds to relative displacements of two distinct atoms. Single particle motions are generally easier to interpret than the relative motion of two distinct particles. One can thus derive most of the relevant dynamical information from incoherent scattering, which has the further advantage to be much more intense. Dynamic analysis of coherent scattering is important with perdeuterated proteins or solutions with D_2O. The neutron scattering experiment determines the statistical average of the phase factors at different times.

This is the self-intermediate scattering function $I_{\mathrm{s},i}(\boldsymbol{Q},t)$ defined for each atom (i) by

$$I_{\mathrm{s},i}(\boldsymbol{Q},t) = \langle \exp(\mathrm{i}\boldsymbol{Q}\boldsymbol{r}_i(0)) \cdot \exp(-\mathrm{i}\boldsymbol{Q}\boldsymbol{r}_i(t)) \rangle \,. \tag{20.2}$$

We omit the cross-sections, since we consider a system of hydrogen atoms, dominating the scattering intensity. The scattering vector $\boldsymbol{Q}$ is an adjustable parameter, which allows to modify the spatial scale probed by the scattering process. $Q = 4\pi/\lambda_n \sin(\theta/2)$ defines its length, λ_n denotes the wavelength of the incident neutrons, and θ is the scattering angle. $I(\boldsymbol{Q},t)$ can be expressed as the Fourier transform of the van Hove self-correlation function in space, $G_{\mathrm{s},i}(\boldsymbol{r},t)$

$$G_{\mathrm{s},i}(\boldsymbol{r},t) = \int \frac{\mathrm{d}^3Q}{(2\pi)^3} \exp(-\mathrm{i}\boldsymbol{Q}\boldsymbol{r}) \cdot I_{\mathrm{s},i}(\boldsymbol{Q},t) \,. \tag{20.3}$$

This even function in space (and time) [17] describes the single particle dynamics of a system averaged over the possible starting points in space. It denotes the probability density, that atom (i) which is initially at $\boldsymbol{r}_0$ moves to a position $\boldsymbol{r}$ within a time interval t. For a classical system it can be written as

$$G_{\mathrm{s},i}(\boldsymbol{r},t) = \int \mathrm{d}^3 r_0 \, p(\boldsymbol{r}_0 + \boldsymbol{r}, \boldsymbol{r}_0, t) \cdot p_0(\boldsymbol{r}_0) \,, \tag{20.4}$$

with the equilibrium distribution

$$p_0(\boldsymbol{r}) = p(\boldsymbol{r}, \boldsymbol{r}_0, t = \infty) \,. \tag{20.5}$$

Thus the Q-dependence of $I_{\mathrm{s},i}(\boldsymbol{Q},\ t_{\mathrm{res}})$ contains the complete information about the single particle dynamics at any fixed instant of time $t = t_{\mathrm{res}}$ (often defined by the energy resolution of the instrument). This argument is stressed because the intermediate scattering function is usually introduced as a correlation function versus time or spectrum versus frequency.

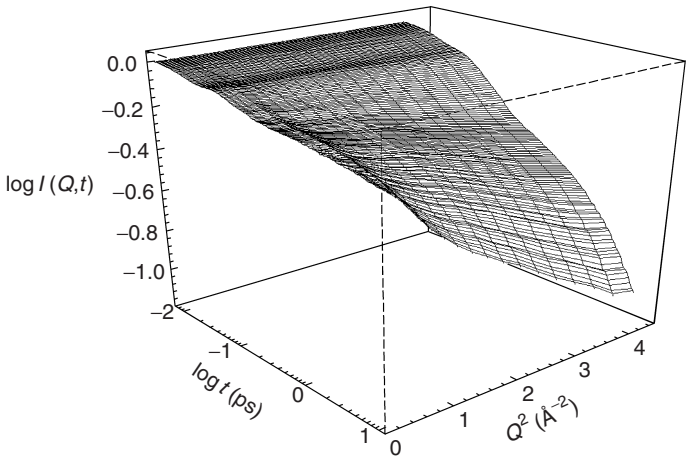

Fig. 20.2. Intermediate scattering function, $I(Q,t)$ of hydrated myoglobin at 300 K, derived by Fourier-deconvolution of the dynamical structure factor $S(Q,\omega)$ (IN6, ILL)

Figure 20.2 shows the experimental Q–t profile of the intermediate scattering function of D_2O-hydrated myoglobin averaged over all atoms (i). The oscillations at short times reflect damped low frequency proteins modes (Boson peak). Two processes with correlation times at 0.3 and 5 ps are visible at high Q correspond to vibrational dephasing and fast water-coupled motions. The variation with Q contains the geometry of the displacements. The decay at $Q = 0$ is due to second-scattering processes, generating a Q-independent quasielastic background (see below).

The interpretation of experimental data becomes most transparent in the case of small Q and/or short times, as can be seen from the expansion of $I_{\mathrm{s},i}(\boldsymbol{Q},t)$ in powers of Q^2

$$I_{\mathrm{s},i}(\boldsymbol{Q},t) = \int \mathrm{d}^3 r \, \exp(-\mathrm{i}\boldsymbol{Q}\boldsymbol{r}) \cdot G_{\mathrm{s}}(\boldsymbol{r},t) \tag{20.6}$$

$$= 1 - \frac{1}{2} \cdot Q^2 \cdot \langle(\hat{Q}\boldsymbol{r})^2\rangle(t) + \frac{1}{24} \cdot Q^4 \cdot \langle(\hat{Q}\boldsymbol{r})^4\rangle(t) - O(Q^6) \tag{20.7}$$

with $\boldsymbol{Q} = Q \cdot \hat{Q}$. This is the moment expansion of the displacement distribution function $G(r,t)$. In the limit

$$Q^2 \cdot \langle(\hat{Q}\boldsymbol{r})^2\rangle(t) \ll 1, \tag{20.8}$$

only the first term of the expansion contributes and two essential consequences arise:

– The correlation function and spectrum are completely determined by the mean squared displacement.

– The intermediate scattering function and dynamic structure factor factorize into a term $\propto Q^2$ and a purely time- or frequency-dependent function, respectively,[1]

$$I(\boldsymbol{Q},t) = 1 - \frac{1}{6}\cdot Q^2 \cdot \langle r^2(t)\rangle, \tag{20.10}$$

$$S(\boldsymbol{Q},\omega) = \delta(\omega) + \frac{1}{6}Q^2 \cdot \mathrm{FT}\left\{-\langle r^2(t)\rangle\right\}(\omega). \tag{20.11}$$

In the following we consider only the self-scattering functions averaged over all atoms. $S(\boldsymbol{Q},\omega)$ denotes the so-called dynamical structure factor, which is the quantity determined by most spectrometers (time-of-flight and backscattering). It is obtained from constant angle cuts at fixed frequency and involves interpolation (see below). The intermediate scattering function is then derived by numerically transforming $S(Q,\omega)$ to the time domain

$$I(Q,t) = \int S(Q,\omega)\exp(\mathrm{i}\omega t)\mathrm{d}(\hbar\omega). \tag{20.12}$$

If the inequality of Eq. 20.8 holds up to a certain time $t_{\max}$, then the Fourier transform is only valid in the set of discrete points

$$\omega_n = n\cdot\frac{\pi}{t_{\max}} \quad \text{for} \quad n \geq 1\,. \tag{20.13}$$

Note also that the measured linewidth of a localized process with time constant τ_{loc} less than $t_{\max}$, i.e.,

$$\langle r^2(t_{\max})\rangle_{\mathrm{loc}} \approx \langle r^2(\infty)\rangle_{\mathrm{loc}} \tag{20.14}$$

is independent of Q and is given by its actual value $\Gamma_{\mathrm{loc}} = 1/\tau_{\mathrm{loc}}$. In addition the squared amplitude of such a process is directly given by the integral over the corresponding quasielastic spectrum. A localized motion or glassy state leads to a long-time plateau of the intermediate scattering function, $\mathrm{EISF}(Q) = I(Q,t\to\infty)$, the so-called elastic incoherent structure factor. Then a purely elastic component (δ-function) arises in $S(Q,\omega)$ at $\omega = 0$. The $\mathrm{EISF}(Q)$ is the Fourier transform of the displacement distribution $G(r,t\to\infty)$. A finite elastic fraction also obtains, if the correlations do not vanish within the time defined by the energy resolution of the spectrometer. With Eqs. 20.4 and 20.5 one obtains the useful relation

$$\mathrm{EISF}(\boldsymbol{Q}) = \left|\int \mathrm{d}\boldsymbol{r}\cdot\exp(\mathrm{i}\boldsymbol{Q}r)\cdot p(\boldsymbol{r}-\boldsymbol{r}_0)\right|^2. \tag{20.15}$$

The elastic fraction, $\mathrm{EISF}(Q)$, thus represents the orientationally averaged (single particle) displacement distribution at infinite time.

[1] Let us – for notational simplicity – assume the usual case of an isotropic sample (not necessarily isotropic dynamics!, see below) which leads to the orientational average of the scalar products in the displacement moments

$$\frac{1}{4\pi}\int \mathrm{d}\Omega\,\langle(\hat{Q}\boldsymbol{r})^{2n}\rangle(t) =: \frac{1}{2n+1}\cdot\langle r^{2n}(t)\rangle. \tag{20.9}$$

20.4 Relevant Time and Spatial Scales

What are the relevant spatial and temporal scales of molecular motions? The shortest time scale is given by the ballistic flight: a particle with mass m is moving with the thermal velocity $v_{\mathrm{th}} = \sqrt{k_{\mathrm{B}}T/m}$ across a distance δ, which requires a time τ_{mic}:

$$\tau_{\mathrm{mic}}^2 = (\delta/v_{\mathrm{th}})^2 = m/(k_{\mathrm{B}}T \cdot Q^2). \tag{20.16}$$

Here the length of the wavevector Q is an experimental parameter, which defines a length scale $Q = 1/\delta$ across which the trajectory of the particle is observed. Ballistic flight is a basic feature of motion in gases, but applies also to molecular motions in liquids and proteins over short times. The corresponding intermediate scattering function is Gaussian [18]

$$I(Q,t) = \exp[-(t/\tau_{\mathrm{mic}})^2] = \exp[-(k_{\mathrm{B}}T/m) \cdot Q^2 t^2]. \tag{20.17}$$

However, liquids and solids unlike gases exhibit a characteristic length scale, the interparticle distance δ. Thus also a characteristic time scale exists

$$\tau_{\mathrm{mic}}^2 = \delta^2 m/(k_{\mathrm{B}}T), \tag{20.18}$$

which is independent of the probing length scale $1/Q$ as in Eq. 20.15. τ_{mic} is typically in the range of 0.5 ps for proteins depending on the mass of the molecular fragments. For times larger than τ_{mic} collective interparticle correlation becomes important, the correlation function deviates from a single exponential decay and the correlation time depends on Q. This regime of complex many-particle interactions is crucial to water-assisted protein flexibility. At long times and large distances in isotropic liquids one enters the hydrodynamic (Gaussian) limit: The correlation time depends on the chosen scale: $\tau^{-1} = D \cdot Q^2$, where D is the diffusion constant of the particle. The corresponding intermediate scattering function is single exponential in time, the quadratic Q-dependence reflects the Gaussian distribution of displacements

$$I(Q,t) = \exp[-Q^2 \cdot D \cdot t]. \tag{20.19}$$

Protein internal coordinates are constrained by covalent and weak forces stabilizing the native state. Long-range diffusion of side-chains is thus prohibited. In Sect. 20.5 we investigate a model of Brownian motion constrained by a harmonic potential.

20.5 The Brownian Oscillator as a Model of Protein-Residue Motion

The harmonic oscillator, driven by random forces of the solvent, has been frequently used as model of protein-residue motion. It is the basic concept

underlying the normal mode analysis of proteins [13, 14]. Mössbauer resonance spectra recording the motion of the heme group were analyzed using a "rugged" Brownian oscillator (BO) model [19]. Surprisingly the BO is not very popular among neutron experimentalists. Instead it is often assumed that protein residues perform free diffusion inside a rigid sphere [20]. The oscillator model does not involve specific assumptions (which are hard to test) and provides a more general perspective. It allows us to pick up the discussion on time and length scales of chap. 19. An example of a Brownian mode analysis was discussed for phycocyanin by Hinsen et al. [21]. Neutron scattering probes the hydrogen atoms attached to the side chains and the main chain. We assume that the amino acid positional fluctuations follow approximately Eq. 20.1 and start with a one-dimensional model: $V(x) = Kx^2$. The harmonic potential implies for the deviations a Gaussian probability distribution. The mean square displacements evolve at high damping monotonically toward an equilibrium value, the average thermal amplitude δ^2 [21, 22]

$$\langle \Delta x^2 \rangle = \delta^2 \cdot (1 - \exp[-2\Gamma_0 \cdot t]). \tag{20.20}$$

The thermal amplitude amounts to $\delta^2 = k_\mathrm{B}T/K$. The relaxation rate is given by $\Gamma_0 = K/f$ and $D = k_\mathrm{B}T/f$ may be interpreted as a diffusion coefficient. Inserting Eq. 20.20 into Eq. 20.6, yields the following intermediate scattering function of the overdamped BO

$$I_\mathrm{B}(Q,t) = \exp[-Q^2\delta^2 \cdot (1 - \mathrm{e}^{-\Gamma_0 t})]. \tag{20.21}$$

The correlation function, $I_\mathrm{B}(Q,t)$, exhibits several interesting features shown in Fig. 20.3. It is nonexponential in time, its effective relaxation time depends on Q and it decays toward a finite plateau at long times the so-called elastic incoherent structure factor, EISF(Q).

$$\mathrm{EISF}(Q) = \exp[-Q^2 \cdot \delta^2] \tag{20.22}$$

Figure 20.3 shows an experimental intermediate scattering function derived from D_2O-hydrated myoglobin [7, 8, 23] covering a wide Q-range. This experiment thus reflects essentially protein structural fluctuations. The harmonic oscillator model fits the data below $Q = 2\,\mathrm{\AA}^{-1}$. But the observed long-time plateau is much higher than predicted by the model at large Q. The spatial constraints of the protein-displacements are thus more severe than those of an isotropic harmonic potential.

The dashed line in Fig. 20.3 was obtained by assuming a two-dimensional harmonic oscillator (see below). The EISF(Q) decreases with increasing spatial resolution (Q) at fixed relaxation rate Γ_0. Since $I_\mathrm{B}(Q,t)$ is not a single exponential one obtains a Q-dependent average relaxation rate according to

$$\frac{1}{\Gamma} = \int_0^\infty \mathrm{d}t (I_\mathrm{B}(Q,t) - I_\mathrm{B}(Q,\infty))/I_\mathrm{B}(Q,\infty). \tag{20.23}$$

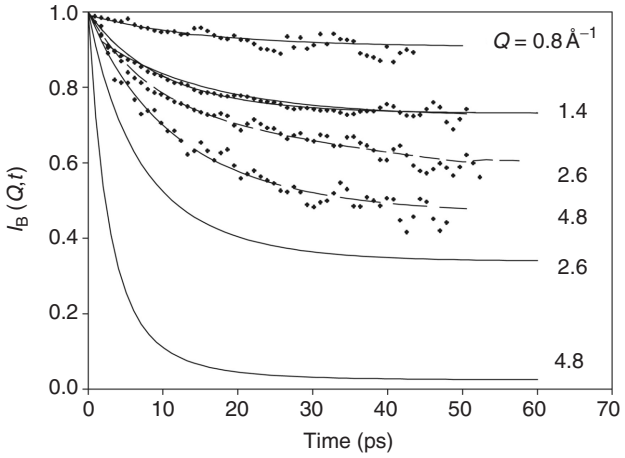

Fig. 20.3. Intermediate scattering function of the BO versus Q (*full line*), Eq. 20.21, and experimental data of D_2O-hydrated myoglobin ($0.35\,g\,g^{-1}$) based on backscattering data (IN13, ILL). Fits (*dashed line*): $\delta = 0.15\,Å^2$, $\Gamma_0^{-1} = \tau_0 = 10\,ps$

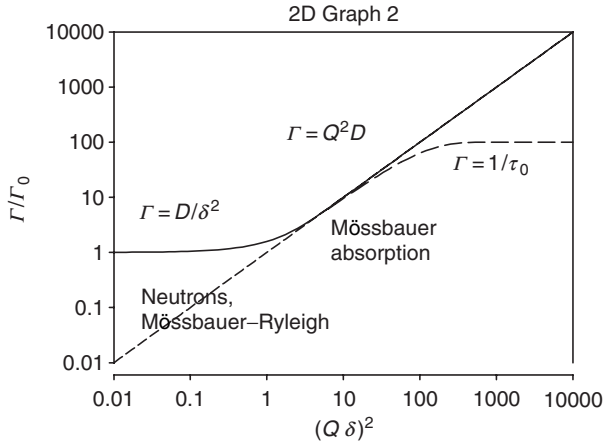

Fig. 20.4. Average relaxation time of the damped harmonic oscillator versus $Q\delta$ Eq. 20.24

Figure 20.4 shows the resulting average rate versus Q. At low Q, the relaxation rate is independent of the spatial scale, the oscillator has explored its entire phase space within a time $\tau = \delta^2/D$. At intermediate Q the displacements are diffusive, $\Gamma \propto Q^2$, while at high Q a limiting rate is achieved reflecting the finite time required for discrete molecular steps. Also indicated in the figure is the experimental range achievable by neutron scattering, Mössbauer absorption spectroscopy and Rayleigh scattering assuming $\delta^2 = 0.2$ Å^2. So

AQ: Please check "Raleigh scattering" is changed to "Rayleigh scattering".

with Mössbauer spectroscopy at $Q = 7\,\mathring{A}^{-1}$ one should observe a much larger rate than for the same oscillator motion at $Q = 2\,\mathring{A}^{-1}$ with neutron scattering.

20.6 The Visco-Elastic Brownian Oscillator

In our simple model we consider conformational fluctuations coupled to fast motions of the solvent, which acts as a heat bath. The BO model of Eq. 20.1 assumes a clear cut separation of time scales between heat bath coordinates and Brownian motion. This allows treating the random force as a δ-correlated Gaussian process (white noise) and the friction coefficient to be time independent. Protein structural fluctuations observed with neutron scattering occur, however, on time scales comparable to solvent dynamics. Thus one has to take into account explicitly the spectrum of random forces, which leads to a time-dependent friction according to the fluctuation-dissipation theorem. The Mori–Zwanzig theory provides an algorithm for the equation of motion, which yields for the density correlator $\Phi_Q(t)$ a generalized oscillator equation containing a time dependent friction kernel $m(t)$, reflecting the slow force correlations [3, 24, 25]. Ω and γ_0 denote a generalized frequency and a regular damping coefficient:

$$\ddot{\Phi}_Q(t) + \Omega^2\Phi_Q(t) + \gamma_0\dot{\Phi}_Q(t) + \Omega^2\int_0^t \mathrm{d}t' m(t-t')\dot{\Phi}_Q(t') = 0\,. \tag{20.24}$$

A general solution to Eq. 20.24 can be given in the frequency domain for the spectrum $S(Q,\omega)$ [3, 18]

$$S(Q,\omega) = -\mathrm{Im}\left\{\frac{\omega + \Omega^2 M(Q,\omega)}{\omega^2 - \Omega^2 + \omega\Omega^2 M(Q,\omega)}\right\}. \tag{20.25}$$

"Im" denotes "imaginary part of" and $\mathrm{i} = \sqrt{-1}$. $M(Q,\omega)$ represents a generalized friction kernel, which can be decomposed into a Newtonian friction γ_0 (collisions) and a slow relaxing part $m_{\mathrm{ps}}(Q,\omega)$ due to protein solvent coupling [25]

$$M(Q,\omega) = \mathrm{i}\gamma_0 + m_{\mathrm{ps}}(Q,\omega). \tag{20.26}$$

To illustrate the basic features of visco-elasticity, we introduce Maxwell's relaxation model. The spectrum of force correlations is Lorentzian in shape, corresponding to an exponential decay of the force correlations [25, 26]

$$m_{\mathrm{ps}}(\tau,\omega) = -F(Q)/(\omega + \mathrm{i}/\tau). \tag{20.27}$$

F is the amplitude and τ denotes the characteristic time of the relaxing friction, which is proportional to the viscosity $\eta = G_\infty \cdot \tau$. G_∞ is the high frequency shear modulus of the liquid. The real part of $\mathrm{m}_{\mathrm{ps}}(\omega\tau)$ contributes to the elastic modulus, while the imaginary part yields a frequency-dependent friction coefficient, $f(\tau,\omega) \propto m''_{\mathrm{ps}}(\tau,\omega)$:

$$\omega m''_{\mathrm{ps}}(\tau,\omega) = F(Q)\cdot\frac{\omega\tau}{1+\omega^2\tau^2}. \tag{20.28}$$

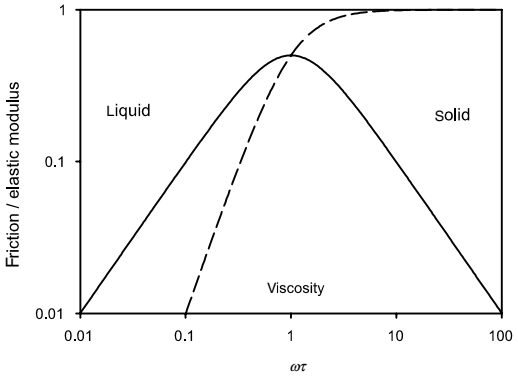

Fig. 20.5. Real (*dashed*) and imaginary part of $\omega m_{\rm ps}(\omega)$ according to Eq. 20.28

The dissipation rate thus assumes a maximum at $\omega\tau = 1$. The friction coefficient vanishes in both limits, $f(\tau \to \infty) \propto \tau^{-1}$ and $f(\tau \to 0) \propto \tau$ at fixed ω as shown in Fig. 20.5. The visco-elastic system thus turns into an elastic solid if the correlation time and thus the viscosity of the heat bath diverges. The same arguments apply to a variation of the frequency at fixed τ. For the simple BO increasing friction will always enhance the viscous properties. As shown in Fig. 20.6a, increasing the damping constant γ leads to a downshift and broadening of the resonance maxima. In the overdamped regime only a narrow central line will remain. In the visco-elastic case, the friction coefficient declines with increasing frequency. Thus even at high viscosity or large τ, an oscillation will persist since $\tau \gg \omega_0^{-1}$.

Experimental neutron scattering spectra behave very much like those in Fig. 20.6b. The vibrational feature near 3 meV has been termed the "boson peak," and involves low frequency oscillations of the protein structure. It is most prominent for large τ (low temperature and high viscosity) and becomes "overdamped" at high temperatures, when the viscoelastic relaxation times are comparable to ω_0^{-1}. A visco-elastic analysis was performed with neutron scattering data of myoglobin [8, 26]. The low-temperature spectrum (150 K) was adjusted to Eq. 20.25, assuming two oscillators as shown in Fig. 20.7. Then by decreasing only the visco-elastic relaxation time τ, the spectrum at 300 K could be simulated. Note that the maximum of Ω_2 is nearly independent of τ in contrast to Ω_1. Note also the difference in position of the boson peak at low temperature between dry and hydrated myoglobin [27].

In this particular experiment we were interested whether the energy of photons absorbed by the heme group of myoglobin was channeled into low frequency vibrations near 30 $\rm cm^{-1}$. Following a laser pulse at 532 nm, we found a simultaneous emission in the far infrared below 50 $\rm cm^{-1}$, suggesting exactly this [26]. The self-friction kernel $\rm m_{ss}(Q, \omega)$ of simple liquids has been calculated on a molecular basis by mode-coupling theory (MCT) [3]. MCT predicts a self-induced structural arrest of the liquid, when the density, depending on

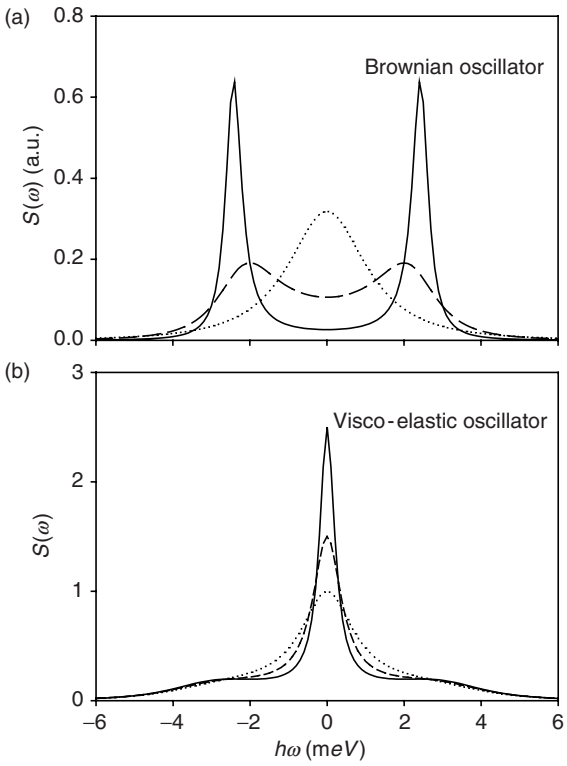

Fig. 20.6. (**a**) Spectrum of a BO: underdamped regime (*full line*), intermediate (*dashed*) and the overdamped case (*dotted*), parameters in meV: $\omega_0 = 2.4, \gamma = 0.5$, 3.0, 6.0. (**b**) spectrum of visco-elastic oscillator (Eq. 20.24), the relaxation time τ increases from *dotted*, *dashed* to *full line*, $F = 1.7$, $\gamma = 0.5$, $1/\tau = 0.5$, 1.0, 2.0 meV. The broadening at $\omega = 0$ is sometimes called the Mountain line

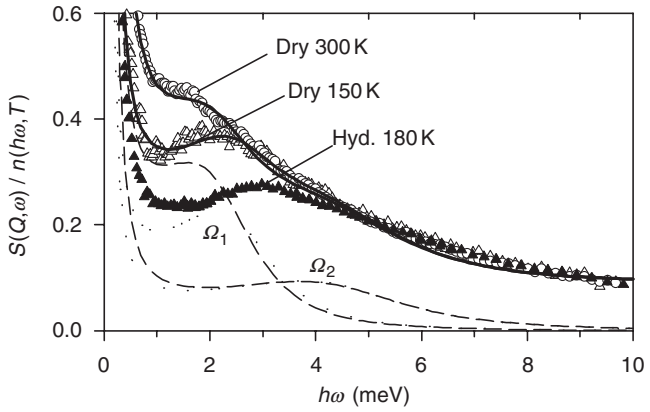

Fig. 20.7. Spectrum of dry and hydrated myoglobin and visco-elastic analysis assuming two oscillators, $\omega_0 = \Omega_1, \Omega_2$ [26]

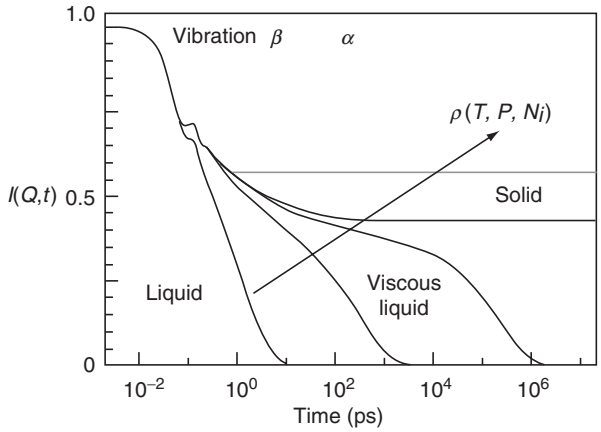

Fig. 20.8. Schematic intermediate scattering function of the generalized MCT-oscillator showing a two-step decay due to fast local (β-process) and slow collective motions (α-process). The oscillatory feature at short times generates the boson-peak in the frequency domain

temperature, pressure, and number concentration, exceeds a critical value. The signature of the glass-transition are nonvanishing density correlations and thus a finite value of the long time intermediate scattering function as shown in Fig. 20.8. MCT approximates the so-called cage effect, each particle is surrounded by a cage of nearest neighbors. Escape out of the cage (the α-process) constitutes the first step leading to long-range diffusion, which is the essence of the liquid state.

Fast local motions (β-processes) can also occur in the glass, but their amplitude (not their rate!) decreases when the density increases. In water, β-processes include hydrogen bond fluctuations and reorientational motions while the α-process involves translation. The glass transition is accompanied by a diverging α-relaxation time, the cage becomes a trap. This reasoning also applies to protein hydration water, which forms a glass at low temperatures [28]. As mentioned in Sect. 20.1, protein residues in a native structure are highly constrained and cannot perform long-range translational displacements. A native protein is not in a liquid state and thus cannot exhibit a liquid to glass transition. However, the protein residues are frictionally coupled to hydration water, which performs a self-induced glass transition at low temperatures [28]. Consequently, water-coupled protein motions will also be arrested because the plasticizer is arrested. Vitrification can also be achieved by cosolvents which seems to be equivalent to dehydration, as Fig. 20.1 shows. Sticking to the generalized oscillator concept, one may introduce the dynamic protein–solvent interactions at the level of the friction kernels

$$m_{\mathrm{ps}}(\omega) \approx m_{\mathrm{p}}(\omega) + m_{\mathrm{ss}}(\omega). \tag{20.29}$$

The internal friction due to water-decoupled structural motions is represented by m_p. With this kernel, water-coupled structural fluctuations will freeze in parallel with the hydration water and behave liquid-like at high temperature. Proceeding in this direction, we have to study the properties of hydration water, which is a true liquid.

20.7 Moment Analysis of Hydration Water Displacements

In the following we analyze experiments performed with H_2O-dehydrated myoglobin in the range of $0.35\,g\,g^{-1}$ degree of hydration. At this level, most of the water is in close contact with the protein surface. The hydration water does not freeze forming ice at low temperatures, instead it vitrifies forming an amorphous structure [28]. Figure 20.9 shows the intermediate scattering function $I(Q,t)$ of water in the hydration shell of H_2O-hydrated myoglobin at various Q-values. It is obtained by Fourier-transforming the spectral function, $S(Q,\omega)$. The amplitude of the fast component at 0.3 ps increases with Q indicating that this component is highly localized. It reflects damped translational oscillations of water molecules. The rate constant of the second process increases with Q (spatial resolution) [29].

This is a characteristic feature of translational diffusion. One expects an exponential correlation function with a characteristic rate $1/\tau = Q^2 \cdot D$ with diffusion constant D. Instead we observe a stretched-exponential decay where

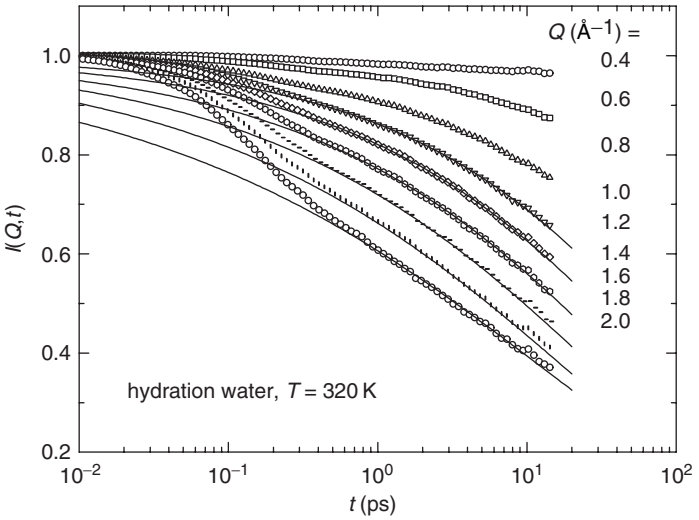

Fig. 20.9. Intermediate scattering function of myoglobin hydration water at $0.35\,g\,H_2O$ per g protein and fits to a stretched exponential function (IN6, ILL) [29]

the diffusion coefficient is Q-dependent [29]

$$I(Q,t) = \exp[-Q^2 \cdot D(Q) \cdot t]^{\beta} = \exp[-Q^2 \cdot \langle r^2(Q,t)\rangle/6]. \qquad (20.30)$$

The stretched behavior, ($\beta < 1$) results from partially localized water molecules at the protein surface. The second equality in Eq. 20.30 refers to a more general property of $I(Q,t)$, which may be expanded in terms of the second and higher moments of the displacement distribution function according to Eq. 20.6

$$I(Q,t) = 1 - A_0(t) - \frac{1}{6}Q^2 \left\langle \boldsymbol{r}^2(t)\right\rangle + \frac{1}{24 \cdot 5} \cdot Q^4 \left\langle \boldsymbol{r}^4(t)\right\rangle - \ldots . \qquad (20.31)$$

Adjusting the data to a fourth-order polynom yields the second and the fourth moment of the displacement distribution function $G(r,t)$. In practice one has to account for multiple scattering corrections $A_0(t)$ [29,30]. Figure 20.10 shows the mean square displacements of protein interfacial water in comparison with bulk water [29]. The data on bulk water by Brockhouse and collaborators provided the first information on fast motions in a liquid using neutron spectroscopy [31]. After the initial rise due to vibrational dephasing, the displacements of bulk water reach the limiting diffusion region ($\left\langle \Delta x^2\right\rangle = 2D \cdot t$), within 10 ps. The slope of the dashed line corresponds to the long time diffusion coefficient of water, $D = 2.45 \cdot 10^{-5}\,\mathrm{cm^2\,s^{-1}}$.

Note the sublinear regime near 1 ps, which reflects the motion of water molecules inside the cage formed by its nearest neighbors. For interfacial water the sublinear range is drastically extended, it takes about 100 ps to reach the

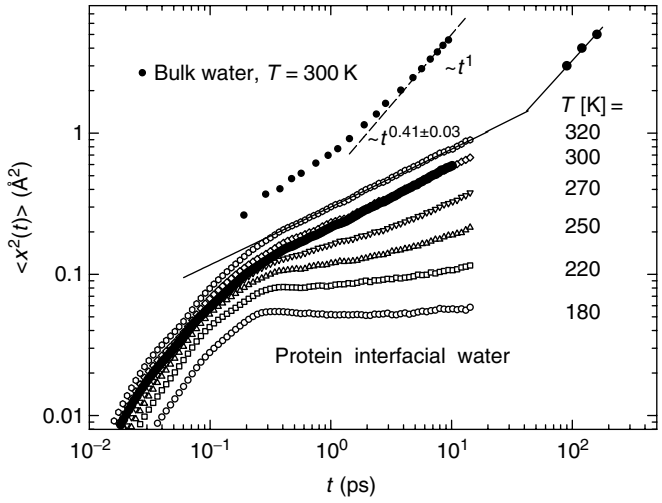

Fig. 20.10. Time-resolved displacements of bulk water and myoglobin interfacial water at 0.4 g D_2O per g protein versus temperature (IN6, ILL; *full circles*: IN15, ILL)

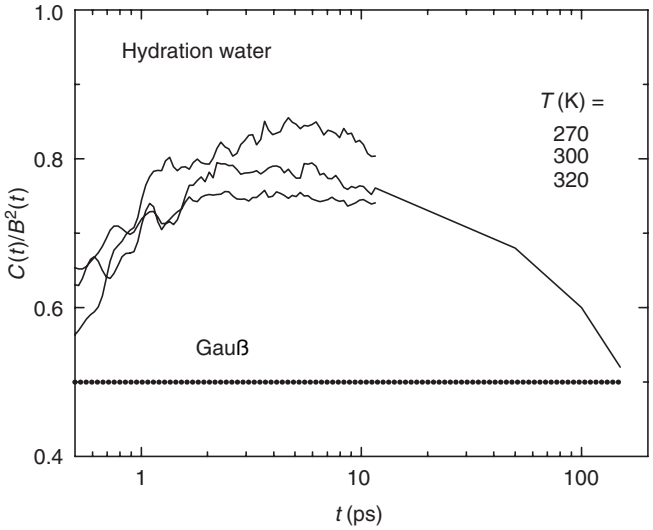

Fig. 20.11. Gauss deviation (fourth moment) of the hydration water displacement distribution versus time of myoglobin ($0.35\,\mathrm{g\,g^{-1}}$)

regime of regular diffusion. The protein thus enhances the cage effect leading to partially localized water states. With decrease in temperature the cage becomes a trap. The extended plateau at 180 K is the signature of a solid state. Structural arrest is achieved continuously as the temperature decreases, which excludes discontinuous transitions such as ice formation.

Figure 20.11 shows the time-dependent fourth moment of the water displacement distribution which is larger than the Gaussian value of 0.5. This indicates that water displacements near the protein surface occur preferentially along a preferred direction. However, at times above 100 ps, the Gaussian value is reestablished, consistent with the observed linear time dependence of the second moment, Fig. 20.10.

20.8 Analysis of Protein Displacements

We now turn to protein motions. As mentioned earlier the relevant spatial information is contained in the Q-dependence of the intermediate scattering function $I(Q,t)$. Figure 20.12 shows this function at fixed $t_{\mathrm{res}} = 50\,\mathrm{ps}$ versus temperature for myoglobin in three environments of Fig. 20.1.

A linear (Gaussian) behavior of $\ln[I(Q)]$ versus Q^2, is observed at low temperatures reflecting vibrational displacements. But above 200 K nonGaussian deviations, first described in [7] become significant. Nearly identical scattering functions are found for the dry and vitrified sample, pointing to similar intramolecular motions. The addition of water has a significant effect on the

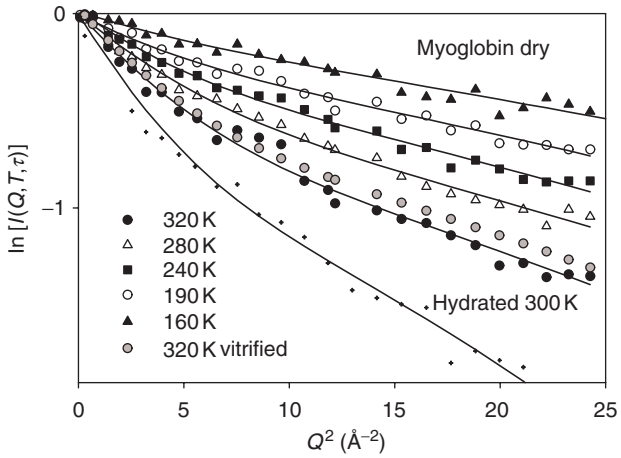

Fig. 20.12. Long time value of $I(Q, t \approx 50\,\mathrm{ps})$ versus Q and temperature for dry myoglobin. Selected data of vitrified and hydrated myoglobin are also shown, *line*: fit to Eq. 20.18, instrument: IN13, ILL

density correlations, indicating water-assisted protein displacements. The simplest model, which fits the data, is a displacement distribution composed of two Gaussians [32, 33]

$$I(Q, T, t_{\mathrm{fix}}) = A_1 \cdot \exp(-Q^2 \left\langle x_1^2 \right\rangle /2) + A_2 \cdot \exp(-Q^2 \left\langle x_2^2 \right\rangle /2). \qquad (20.32)$$

Figure 20.13 shows the second moments of the two Gaussian components determined on absolute scale [7, 10].

The first component has a plateau at low temperatures given by the protein zero point vibrations $(0.014(\pm 0.002)\,\mathrm{Å}^2$. This component shows harmonic behavior across the whole temperature range in the case of the dehydrated and the vitrified system. However, in the hydrated system an additional increase occurs above 240 K due to water-assisted motions. In contrast the second component emerges above 150 K and leads to a nonlinear enhancement in the total displacements independent of the protein environment. Figure 20.14 shows that the corresponding displacement distribution of hydrated myoglobin at fixed time versus temperature, $4\pi\ r^2 G(r, T, t = 50\,\mathrm{ps})$. Component 1 broadens with increasing temperature due to vibrational motions. But above 240 K the maximum is shifting and the width increases. This effect points to small scale continuous motions. It is seen only with hydrated samples. In contrast, component 2 is observed in all samples independent of the protein environment. It has its maximum near 1.5 Å, indicating large scale excursions.

What is the molecular nature of the two types of motions? Several authors have emphasized the relevance of dynamical heterogeneity in the context of neutron scattering experiments [33, 34]. With neutron scattering we probe, because of their large cross-section, the trajectories of nonexchangeable

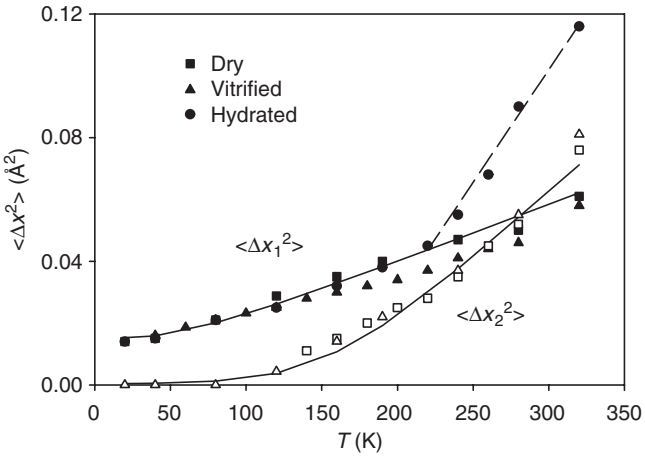

Fig. 20.13. Second moment of the displacement distribution (myoglobin, dry, d-glucose-vitrified and hydrated ($0.4\,\mathrm{g\,g^{-1}}$) at a fixed time of 50 ps, derived from data in Fig. 20.12, *closed symbols*: harmonic component, *open symbols*: total displacements, lines: from fits in Fig. 20.12, (instrument: IN13, ILL)

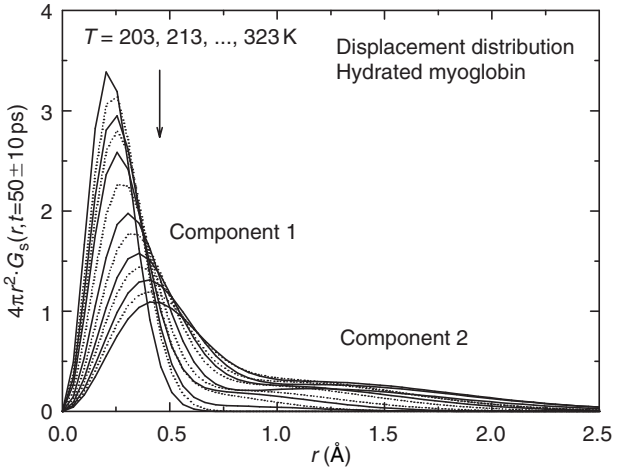

Fig. 20.14. Displacement distribution (myoglobin, D_2O-hydrated ($0.4\,\mathrm{g\,g^{-1}}$) at a fixed time of 50 ps versus temperature derived from data in Fig. 20.12, (instrument: IN13, ILL)

hydrogens, which are attached to the protein side-chains and, to a minor fraction, to the main chain. As discussed above structural changes of the protein chain involve mostly rotational jumps, while displacements in liquids are more continuous and on a small scale. Rotational jumps of methyl groups and of

heavy atom dihedral transitions are the most natural modes of motion of a polypeptide chain. Moreover, the partial cross-section due to methyl groups is about 25%, which is the most significant individual contribution. Since we know its partial cross-section, the structure factor and the barrier to rotation from energy-resolved experiments one can calculate the scattering function without adjustable parameters. The results are shown as the solid lines in Fig. 20.12 and 20.13. The average rotational barrier of methyl groups in myoglobin amounts about $10\,\mathrm{kJ\,mol^{-1}}$. The increase in the apparent displacements due to component 2, $\langle \Delta x^2 \rangle_2$, in Fig. 20.13 most likely results from an increasing rotational rate at fixed instrumental resolution (50 ps). A low temperatures the apparent displacement of component 2 is zero because the transitions are too slow to be resolved by the instrument. The slight discrepancy between the data and the theoretical curve at low temperatures may indicate a distribution of rates. The close agreement with experimental data produced by this model suggests strongly that rotational transitions, essentially of methyl groups, are the origin of the nonGaussian displacement distribution. Dynamical heterogeneity seems to be of minor importance. Rotation of methyl groups occurs in the hydrated, the dry as well as in the vitrified state. Water induces additional small scale protein displacements, which appear as anharmonic enhancements of the vibrational component 1.

20.9 Data Analysis

High resolution instruments collect data at constant angle and not at constant Q in contrast to three-axis spectrometers. As a result one has to transform the experimental data from a "constant angle" to a "constant Q" format: The momentum exchange, $\Delta \boldsymbol{p} = \hbar \boldsymbol{Q}$, at fixed angle, varies with the energy transfer $\hbar\omega$, according to [17]

$$Q^2 = \frac{2m_\mathrm{n}}{\hbar^2}(2E_0 + \hbar\omega - 2\cos(\theta) \cdot \sqrt{E_0(E_0 + \hbar\omega)}). \tag{20.33}$$

To determine the physically relevant quantity $S(Q, \omega)$ based on $S(\theta, \omega)$ data involves extrapolation and interpolation as indicated in Fig. 20.15. Only the area of the kinetic plane enclosed by the lines contains experimental data. Figure 20.16 illustrates for a particular case, how the "constant angle" data differ from the final interpolated "constant-Q" spectrum.

The low-Q regime, which is quite important to data analysis, is hampered by two difficulties; the necessity to extrapolate finite Q data and the relevance of multiple scattering. Multiple scattering tends to generate a Q-independent inelastic background [35]. Figure 20.17 shows that even for a thin sample with 91% transmission about 15% of the incident neutrons are multiply scattered.

AQ: Please check that "mwV" is changed to "meV".

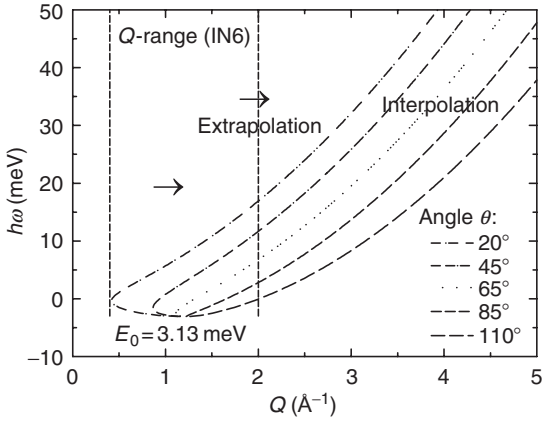

Fig. 20.15. Kinetic plane for an incident neutron wavelength of 5.1 Å or $E_0 = 3.13$ meV. Only the area enclosed by the lines is accessible to the experiment. Constant-Q data can be calculated from constant angle experiments by interpolation. To reach the low Q range, extrapolation is required [30]

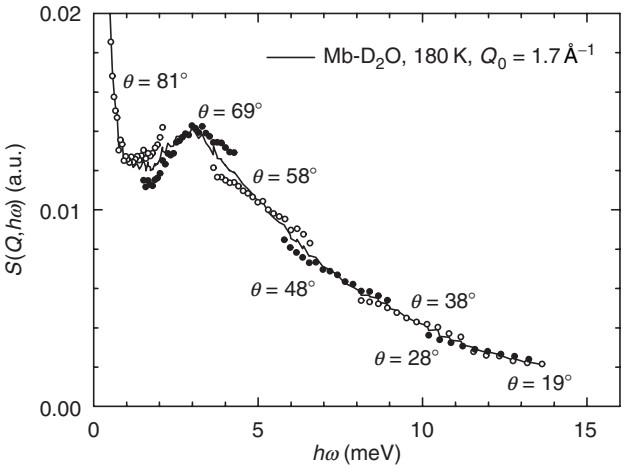

Fig. 20.16. Experimental "constant angle" (θ) neutron scattering spectra of myoglobin (IN6, ILL) and interpolated "constant Q" spectrum. The "elastic" $Q = Q_0$ at $E = E_0$ was 1.7 Å^{-1} [30]

A very detailed analysis always requires consideration of multiple scattering. An initial estimate is the Q-independent background extrapolated to $Q = 0$. Then the corrected spectrum can be used to calculate the multiple scattering corrections iteratively. This is particularly relevant to high-frequency data [30].

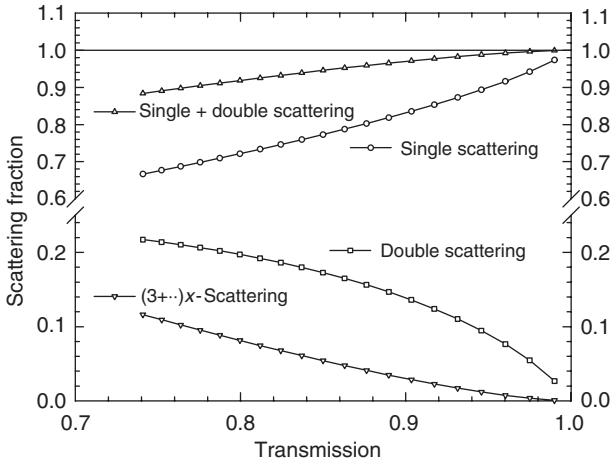

Fig. 20.17. Multiple scattering fraction versus sample transmission calculated for an infinite, thin slab sample holder inclined at 135° relative to the beam [17, 30]

20.10 Conclusions

Dynamic neutron scattering provides a unique tool to probe the statistical properties of picosecond motions in biomolecules. To understand the effect of water on structure and stability of proteins requires to study the interactions on the time scale where hydrogen bonds are broken and formed. INS thus complements other local methods like NMR and fluorescence emission. We suggest to assume a general perspective without resigning too early to particular models: A moment analysis of scattering data leads to model-independent insight into molecular mechanisms. It requires, however, high quality data. Two classes of protein displacements could be discriminated: torsional transitions and water-assisted motions. The latter are composed of fast H-bond fluctuations and slower small scale displacements. The dynamical transition is driven by the H-bond dynamics of hydration water [10,28,36], which has, however, minor effects on the rotational transitions. The transition temperature thus varies with H-bond strength and viscosity [37]. Within a glass-transition scenario our results support the notion of water-plasticized β-processes in proteins proposed by Green and Angell [11]. A quite interesting perspective is to study the real time protein–water coupling processes using generalized harmonic oscillator models. Structural rearrangements correlated with motions of water molecules occur on a time scale of picoseconds. In what sense is then the fast motion of water molecules relevant to the observed slow substrate conversion in enzymes? For myoglobin, it could be shown, that the solvent modulates the barrier which controls ligand entry and escape according to Kramers law of activated escape [37,38]. The solvent generates the "seascape" of fluctuating barriers. This does not imply, that protein activity occurring on a time scale

of seconds vanishes, because of reduced picosecond structural fluctuations as suggested in [39]. The essential dynamical quantity is the solvent viscosity (Eq. 20.1), which was not taken into account in [39]. The displacements of molecules on a microscopic scale including water molecules in the active site are discontinuous and always fast. The millisecond time scales come about by high energetic or entropic barriers which prevent particular rearrangements for long-time intervals. Enzymes are thus devices, which select by construction a small fraction of events out of a large number of fast structural fluctuations.

Acknowledgments

The author is grateful for technical support by the instrument responsibles of the Institut Laue Langevin and the collaboration with many colleagues, in particular with Marcus Settles, who rediscovered the moment method for biology. Financial support by the Bundesministerium für Bildung und Forschung (grant 03DOE2M) is gratefully acknowledged.

References

1. K.A. Dill, Biochemisby **29** (1990), 7132–7155
2. W. Doster, M. Diehl, H. Leyser, W. Petry, H. Schober, in *Spectroscopy of Biological Molecules* J. Greve, G.J. Puppels, C. Otto (Eds.) (Kluwer, Dordrecht, 1999) pp. 655–659
3. W. Göetze, L. Sjögren, Rep. Prog. Phys. **55** (1992), 241–376
4. J. Fitter, R. Lechner, G. Büldt, N.A. Dencher, Proc. Natl Acad. Sci. USA **93** (1996), 7600–7605
5. U. Lehnert, V. Reat, M. Weik, G. Zaccai, C. Pfister, Biophys. J. **75** (1998), 1945–1952
6. M.C. Bellissent-Funel, J.M. Zanotti, S.H. Chen, Faraday Discuss. **103** (1996), 281–294
7. W. Doster, S. Cusack, W. Petry, Nature (London) **337** (1989), 754
8. W. Doster, S. Cusack, W. Petry, Phys. Rev. Lett. **65** (1990), 1080
9. M. Tarek, D. Tobias, Mod. Phys. Lett. B **5** (1991), 1407
10. W. Doster, M. Settles, in *Hydration Processes in Biology, Protein Dynamics, The Role of Hydrogen Bonds*, Nato Science Series A Life Science, Vol. **305** (IOS Press, Amsterdam, 1998), pp. 177–194
11. J.L. Green, J. Fan, A. Angell, J. Phys. Chem. **98** (1994), 13780–13790
12. W. Doster, M. Settles, Biochim. Biophys. Acta **1749** (2005), 173–186
13. A. Kitao, F. Hirata, N. Go, Chem. Phys. Lett. **158** (1991), 447–472
14. S. Hayward, A. Kitao, F. Hirata, N. Go, J. Mol. Biol. **234** (1993), 1207–1217
15. G. Kneller, Chem. Phys **261** (2000), 1–24
16. F. Mezei, in *Liquids, Freezing and The Glass Transition*, J.P. Hansen, D. Levesque, J. Zinn-Justin (Eds.) (Elsevier, Amsterdam, 1991, Les Houches, 1989), pp. 632

17. M. Bee, *Quasielastic Neutron Scattering* (Adam Hilger, Bristol, Philadelphia, 1988), p. 16
18. W. Marshall, S.W. Lovesey, *Theory of Thermal Neutron Scattering* (Clarendon, Oxford, 1971)
19. F. Parak, E.W. Knapp, D. Kucheida, J. Mol. Biol. **161** (1982), 177–194
20. D.J. Bicout, Phys. Rev. E. **62** (2000), 261–271
21. K. Hinsen, A.J. Petrescu, S. Dellerue, M.C. Bellissent-Funel, G.R. Kneller, Chem. Phys. **261** (2000), 25–37
22. G.E. Uhlenbeck, L.S. Orstein, Phys. Rev. **36** (1930), 823–829
23. W. Doster, (unpublished)
24. J.B. Boon, S. Yip, *Molecular Hydrodynamics*, (McGraw-Hill, New York, 1980)
25. W. Göetze, L. Sjögren, Trans. Theory Stat. Phys. **24** (1995), 801–853
26. H. Leyser, W. Doster, M. Diehl, Phys. Rev. Lett. **82** (1999), 2897
27. M. Diehl, W. Doster, W. Petry, H. Schober, Biophys. J. **73** (1997), 2726–2732
28. W. Doster, T. Bachleitner, M. Hiebl, E. Lüscher, A. Dunau, Biophys. J. **50** (1986), 213–219
29. M. Settles, W. Doster, Faraday Discuss. **103** (1996), 269–279
30. M. Settles, W. Doster, in *Biological Macromolecular Dynamics*, H. Büttner et al. (Eds.) (Adenine, New York, 1996), pp. 307–331
31. M. Sakamoto, B.N. Brockhouse, R.G. Johnson, N.K. Pope, J. Phys. Soc. Jpn **17** (1962), 370–376
32. M. Settles, Thesis (Technical University Munich, Munich, 1997)
33. H. Nakagawa, H. Kamikubo, I. Tsukushi, T. Kanaya, M. Kataoka, J. Phys. Soc. Jpn **73** (2004), 491–495
34. J.A. Hayward. J. Smith, Biophys. J. **82** (2002), 1216
35. S. Cusack, W. Doster, Biophys. J. **58** 1990, 243–251
36. M. Tarek, D. Tobias, Phys. Rev. Lett. **88** (2002), 138101
37. H. Lichtenegger, W. Doster, T. Kleinert, B. Sepiol, G. Vogl, Biophys. J. **76** (1999), 414–422
38. T. Kleinert, W. Doster, H. Leyser, W. Petry, V. Schwarz, M. Settles, Biochemistry **37** (1998), 717–733
39. R.M. Daniel, J. Smith, M. Ferrand, S. Hery, R. Dunn, J. Finney, Biophys. J. **75** (1998), 2504

AQ: Please provide more information for Ref. [23].